

<https://doi.org/10.1038/s43247-025-02876-z>

Abundant high-pressure minerals and submicroscopic metallic iron discovered in a shocked lunar meteorite

Check for updates

Lixin Gu^{1,2}✉, Nian Wang², Yangting Lin²✉, Hengci Tian², Xu Tang^{1,2}, Zhan Zhou², Xiaoguang Li¹, Lihui Jia¹, Yuchen Xu³, Sen Hu² & Jinhua Li^{4,5}✉

Although the Moon's surface is covered by countless impact craters, high-pressure phases are rare in lunar samples, limiting our understanding of impact history and their associated shock effects. Here we report abundant high-pressure minerals in the highly shocked lunar meteorite Northwest Africa 3170, six of which are found for the first time in lunar samples, including ahrensite, tuite, xieite, majorite, majorite-pyrope and vitrified bridgmanite, in addition to previously identified phases such as stishovite, seifertite, and ringwoodite. This mineral assemblage indicates intense shock metamorphism (~22–24 GPa and ~2000 °C) and rapid cooling (quench time < 15 ms). Notably, substantial amounts of submicroscopic metallic iron were generated during impact rather than through space weathering, implying that large-scale impacts may have contributed significantly to metallic iron on the Moon. These findings offer new perspectives on the impact history of the Moon and the behavior of materials under extreme conditions.

Large-scale impact events played a vital role in the formation and evolution of the Moon, evidenced by the dense distribution of impact basins and craters on its surface. The transient high pressures and temperatures produced during an impact induce various shock effects on the minerals, such as melting, vaporization, mechanical deformation, and high-pressure phase transformation^{1,2}. However, compared with highly shocked ordinary chondrites and Martian meteorites, lunar samples appear to contain fewer high-pressure phases, limiting our understanding of the large-scale shock effects on the Moon^{3,4}. Reported high-pressure phases include high-pressure polymorphs of olivine (ringwoodite and wadsleyite)^{5,6}, silica (coesite, stishovite, and seifertite)^{7–12}, zircon (reidite)⁴, plagioclase (tissintite)^{13,14}, and Ca-Al-silicate (donwilhelmsite)¹⁵. Most of these high-pressure phases are primarily observed as isolated occurrences within or near shock-induced melt veins.

The Moon's surface is covered by a layer of fine-grained regolith. The regolith is constantly altered in both physical and compositional properties by space weathering processes—driven predominantly by micrometeoroid impacts and solar wind irradiation^{16–21}. Notably, nanophase metallic iron (npFe⁰) particles, an important product of space weathering, could be responsible for the spectral properties of lunar regolith^{16,22,23}. However, other

types of space environmental effects may also play a role, including the crystallization of lunar basalt in low oxygen fugacity conditions²⁴, the addition of meteoritic metals (Fe or FeNi)²⁵, or larger-scale meteoroid impacts²¹, and the contribution of these processes is still being investigated.

Northwest Africa (NWA) 3170 is a lunar breccia containing clasts of various lithologies, including olivine gabbro, ferroan gabbro, anorthositic gabbro, and polymict breccia^{26–28}. It is inferred to be paired with the NWA 773 clan, which is KREEP-like and shows distinct geochemical characteristics from the samples collected by sample return missions²⁹. In-situ dating of baddeleyite, zircon, and apatite has primarily yielded Pb-Pb (or U-Pb) ages of approximately 3.1 Ga²⁶, indicating that these rocks represent relatively young lunar igneous rocks. The igneous material was mixed with breccia components before being ejected from the Moon³⁰. In this study, a detailed mineralogical investigation of NWA 3170 was conducted using a series of advanced analytical techniques, including scanning and transmission electron microscopy and Raman spectroscopy. Our results offer unequivocal evidence of abundant high-pressure polymorphs and submicroscopic metallic iron in NWA 3170. They reveal the strongest shock metamorphism in lunar samples and provide unique insights into the shock processes and effects associated with large-scale impact events.

¹Institutional Center for Shared Technologies and Facilities, Institute of Geology and Geophysics, Chinese Academy of Sciences, Beijing, China. ²Key Laboratory of Earth and Planetary Physics, Institute of Geology and Geophysics, Chinese Academy of Sciences, Beijing, China. ³State Key Laboratory of Space Weather, National Space Science Center, Chinese Academy of Sciences, Beijing, China. ⁴Key Laboratory of Deep Petroleum Intelligent Exploration and Development, Institute of Geology and Geophysics, Chinese Academy of Sciences, Beijing, China. ⁵College of Earth and Planetary Sciences, University of Chinese Academy of Sciences, Beijing, China. ✉e-mail: gulixin@mail.iggcas.ac.cn; LinYT@mail.iggcas.ac.cn; ljjinhua@mail.iggcas.ac.cn

Results

The NWA 3170 meteorite investigated in this study comprises olivine gabbro and polymict breccia lithologies (Supplementary Fig. S1). The olivine gabbro is primarily composed of olivine, pigeonite, augite, and anorthite (Supplementary Table S1). Some minerals show various shock features such as dislocations, twinning, and planar microcracks. Accessory minerals, including fayalite, silica, spinel, and phosphates, are mainly concentrated in the polymict breccia. The presence of shock melt veins in the breccia and at its boundary with the olivine gabbro indicate intense shock metamorphism (Supplementary Fig. S1). The widths of the shock melt veins are approximately 2–120 μm , and their lengths vary significantly, with the longest exceeding 10 mm (Supplementary Fig. S1). Shock-induced glasses, including maskelynite and pyroxene glass, were identified based on their Raman spectra (Supplementary Fig. S2). Additionally, we also identified abundant occurrences of high-pressure polymorphs in or at the rim of shock melt veins.

Stishovite was identified near the melt veins and pockets, as evidenced by its characteristic Raman peaks at ~ 232 and 756 cm^{-1} (Supplementary Fig. S3)³. It exhibits subhedral textures with grain sizes of up to $2\text{ }\mu\text{m}$ (Supplementary Fig. S3a). Some pyroxene fragments are enclosed in the adjacent silica glass (Supplementary Fig. S3b). Additionally, some silica grains display a tweed-like texture, indicative of transformation into seifertite ($\alpha\text{-PbO}_2$ -type SiO_2), which features diagnostic Raman peaks at 378 and 511 cm^{-1} (Supplementary Fig. S3e)³¹. The presence of shock melt residue was observed in the seifertite grain, as shown in Supplementary Fig. S3c.

Ringwoodite and ahrensite, the Mg- and Fe-end-members of $\gamma\text{-(Mg, Fe)}_2\text{SiO}_4$, were identified within and near the melt veins (Fig. 1a), with a strong characteristic Raman peak around 842 cm^{-1} (Fig. 1c)^{32,33}. Olivine with an Fa content of 28 ($100\times\text{Fe}/(\text{Fe}+\text{Mg})$, atomic ratio) in contact with the melt vein was completely transformed into ringwoodite, exhibiting a significantly different contrast (Fig. 1a). The identified ahrensite grains had higher Fa values (Fa > 97, composition of Ahr-1 and Ahr-2 presented in Supplementary Table S2) and featured three occurrences: (1) completely transformed into ahrensite adjacent to the melt vein (Fig. 1b); (2) as ahrensite lamella in the fayalite (Fig. 1d); and (3) as sub- μm granular ahrensite clusters in the melt-vein matrix (Fig. 1e). The Raman peak at 668 cm^{-1} (R216 and R574 in Fig. 1c) may correspond to the bridgmanite that was vitrified under decompression, similar to those observed in some Martian and chondrite meteorites^{34,35}. Additionally, in the first occurrence, large amounts of bright nanoparticles coexisting with polycrystalline ahrensite were observed in the magnified scanning electron microscopy (SEM) image (Fig. 2a). Subsequently, we prepared an ultrathin foil (Foil 1) for further structural analysis. The HAADF image and its corresponding EDS maps revealed that these nanoparticles were rich in Fe but poor in O (Fig. 2c–e). Quantitative TEM-EDS analysis of one nanoparticle showed an Fe content of 74 wt% with small amounts of Si and O, which may be influenced by the surrounding ahrensite (composition of Foil 1 is presented in Supplementary Table S3). The HRTEM image and corresponding fast Fourier transform (FFT) analyses confirmed that these nanoparticles were metallic iron (Fig. 2g).

Tuite, a high-pressure polymorph of Ca-phosphate with the structure of $\gamma\text{-Ca}_3(\text{PO}_4)_2$, was discovered near the shock melt vein (Fig. 1b), exhibiting a strong Raman peak at 973 cm^{-1} (R214 in Fig. 1c)³⁶. Additionally, xieite, a high-pressure polymorph of chromite (CaTi_2O_4 -type structure), was identified in direct contact with the melt vein (Supplementary Fig. S4). Xieite shows significantly different Raman spectral characteristics from chromite (Supplementary Fig. S4b). The corresponding EBSD pattern matched well with the xieite structure (an orthorhombic phase characterized by cell parameters of $a = 2.88\text{ }\text{\AA}$, $b = 9.52\text{ }\text{\AA}$, $c = 9.75\text{ }\text{\AA}$)³⁷, with a mean angular deviation (MAD) of 0.77 (Supplementary Fig. S4c). Xieite grains exhibit a preferred orientation (Supplementary Fig. S4e) and have a similar composition to the adjacent chromite (Supplementary Table S2). Some lamellae observed slightly away from the shock vein were likely chenmingite that were formed at lower temperatures (Supplementary Fig. S4a)³⁸.

Exsolution lamellae comprising high- and low-Ca components are prevalent in pyroxenes. However, some low-Ca lamellae near the melt vein appeared brighter (Fig. 3a), displaying a strong Raman peak at 916 cm^{-1} (R284 in Fig. 3e) that was clearly distinct from those peaks at 671 and 1002 cm^{-1} for the adjacent pyroxene (R286 in Fig. 3e). The Raman peak at 916 cm^{-1} can be attributed to a garnet-like mineral³⁹, whereas that at 667 cm^{-1} corresponds to bridgmanite glass^{34,35}. The foil (Foil 2) was extracted for TEM analysis. Both the HRTEM image and SAED pattern were consistent with a low-Ca majorite (garnet) structure (Fig. 3d). The presence of weak $\{h0l\}$ reflections (where $h, l = \text{odd}$) suggested that the space group featured tetragonal symmetry ($I4_1/a$) rather than cubic symmetry ($Ia\bar{3}d$)^{35,40}. However, high-Ca lamellae still exhibited a monoclinic pyroxene structure, as demonstrated from the identical SAED patterns at different areas (Fig. 3f).

Majorite-pyroxene solid solution, a major rock-forming mineral in the upper mantle and transition zone of the Earth⁴¹, was observed as granular crystals within the melt vein, with diameters ranging from a few hundred nanometers to several micrometers (Fig. 4a). They had a characteristic Raman peak at around 918 cm^{-1} (R571 in Fig. 4b), and their structure can also be confirmed by SAED patterns along the $[110]$ and $[111]$ zone axes (Fig. 4f, h). Some grains exhibited distinct compositional zoning in the BSE (Fig. 4a) and HAADF images of extracted ultra-foil (Supplementary Fig. S5) owing to the fast cooling rate^{35,42}. Additionally, fine-grained Fe-rich particles were observed both within majorite-pyroxene (Fig. 4d–e) and the matrix (Fig. 4h–j). These particles comprised subgrains, including metallic iron ($\alpha\text{-Fe}$) and iron-sulfide (Fig. 4e, and Supplementary Figs. S5 and S6). Semi-quantitative TEM-EDS analysis of these nanoparticles showed an iron concentration of up to 85 wt% and a small amount of adjacent material (compositions of Foil 3 and Foil 4 are presented in Supplementary Table S3). The metallic iron and iron-sulfide assemblage in Foil-3 extracted from the center of the melt vein contains approximately 2 wt% Ni, whereas the metallic iron in Foil-4 extracted near the edge of the melt vein contains no detectable Ni. The structure of metallic iron can be confirmed in high-resolution TEM images (Fig. 4g) and CBED patterns (Fig. 4j), with measured d-spacings of approximately 2.05 and $1.18\text{ }\text{\AA}$ (insets of Fig. 4g, j), which are consistent with the (110) and $(\bar{1}21)$ planes of the metallic iron ($\alpha\text{-Fe}$) phase, respectively.

Discussion and implications

High-pressure phase transformation

Various high-pressure minerals were observed in the shock veins of NWA 3170, including stishovite, seifertite, ringwoodite, ahrensite, tuite, xieite, majorite, majorite-pyroxene, and vitrified bridgmanite, to the best of our knowledge, six of which are reported for the first time in lunar samples (Table 1). This suggests that substantial amounts of high-pressure minerals can also be produced and well-preserved in lunar samples.

It has been extensively demonstrated that high-pressure minerals form either by solid-state transformation of low-pressure polymorphs or crystallization from shock melts^{3,43,44}. In this study, some of these high-pressure phases, such as ringwoodite and xieite, are definitively formed through a solid-solid phase transformation, as inferred from their occurrences and similar composition to the host minerals (Supplementary Table S2). Tuite has a relatively high FeO content, and no apatite or Cl- or F-bearing minerals were found nearby. Therefore, it is very likely formed through the solid-state phase transformation of merrillite rather than by the decomposition of apatite^{31,45,46}. Majorities formed by either solid-state transformation or melt crystallization have been documented in many ordinary chondrites and Martian meteorites^{3,47}. However, in this study, we presumed that the low-Ca majorite identified here should have been formed by the solid-state transformation of low-Ca pyroxene, as evidenced by the parallel exsolution lamellar texture (Fig. 3b). Such occurrence of majorite has never been reported in previous studies.

Ahrensite, with both polycrystalline and lamellar textures, was observed in the host fayalite grains (Fig. 1b–d), indicating a solid-solid phase transition⁴⁸. However, ahrensite clusters in the melt vein (Fig. 1e) likely

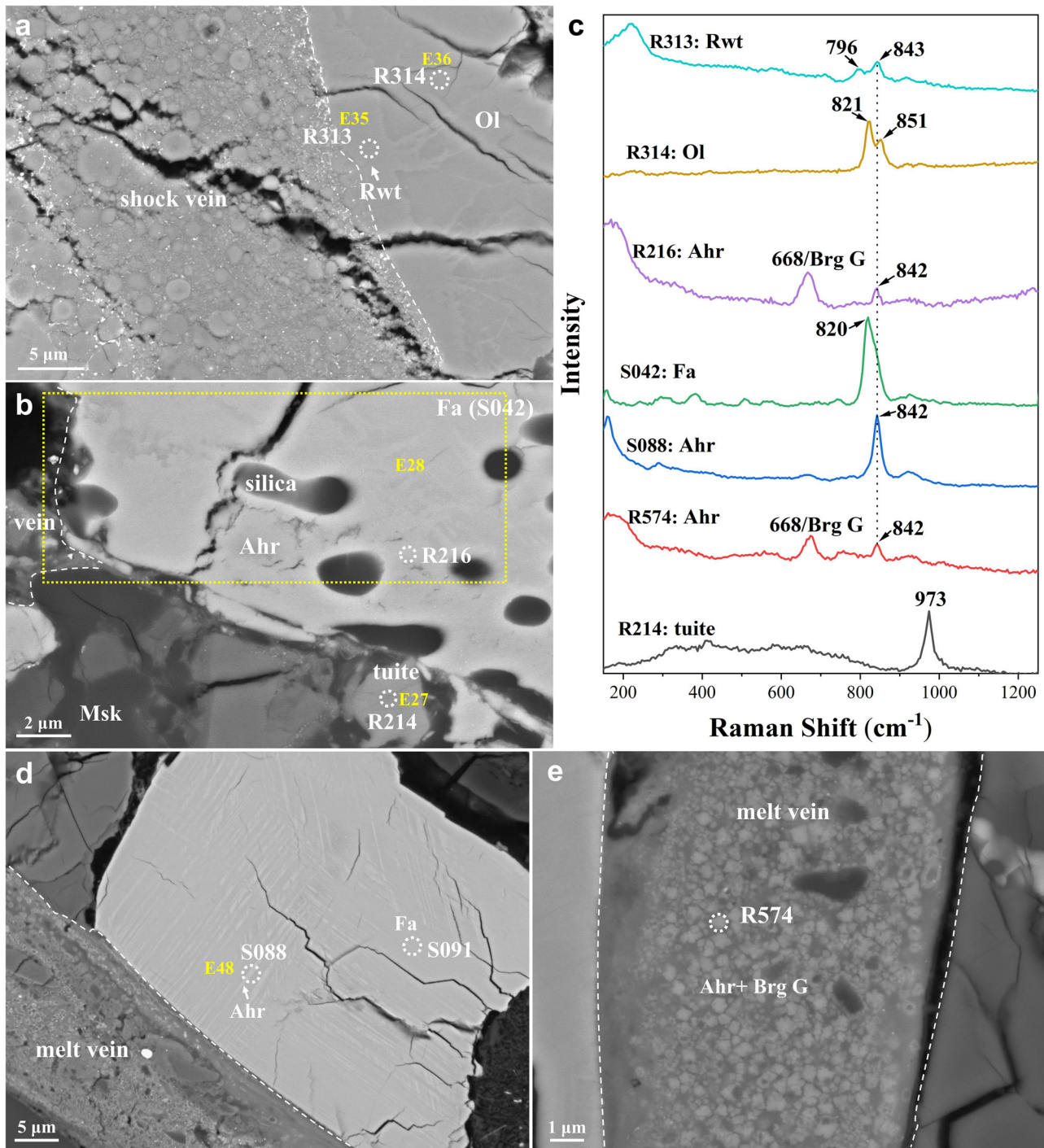


Fig. 1 | Occurrences of ringwoodite, ahrensite and tuite. a BSE image of ringwoodite in contact with the longest shock-induced melt vein. **b** BSE image of ahrensite and tuite near the melt vein. **c** Raman spectra of various minerals. **d** Lamellar ahrensite near the melt vein. **e** BSE image of ahrensite + vitrified

bridgmanite in the melt vein. Rwt ringwoodite, Ol olivine, Ahr ahrensite, Fa fayalite, Msk maskelynite, Brg G bridgmanite glass. Yellow markers (e.g., E35) indicate the positions of EPMA measurements. White lines indicate the boundaries of the melt veins.

crystallized from the shock melt⁴⁹. Similarly, the majorite-pyrope should have also crystallized from the shock melt, as evidenced by its granular morphology and internal sulfides (Fig. 4). Moreover, we observed some mineral fragments in the silica glass beside stishovite and melt residues in the seifertite grain (Supplementary Fig. S3c), indicating that some stishovite and seifertite crystallized from the shock melt. However, the formation mechanism of most high-pressure phases of silica is difficult to determine. Apart from the high-pressure phases, we only observed some silica glass. Considering that most silica grains in lunar meteorites and Apollo samples

are cristobalite, we cannot rule out the possibility that some high-pressure phases of silica may be formed by solid-state transitions, as reported in other lunar samples^{8,9}.

Shock condition constraints

The unique assemblage of high-pressure phases and shock features in NWA 3170 can be used to estimate the pressure and temperature (P–T) conditions of its shock metamorphism (Supplementary Fig. S7). Previous studies have suggested that pyroxene glasses form under shock pressures of 26–35 GPa⁴⁹.

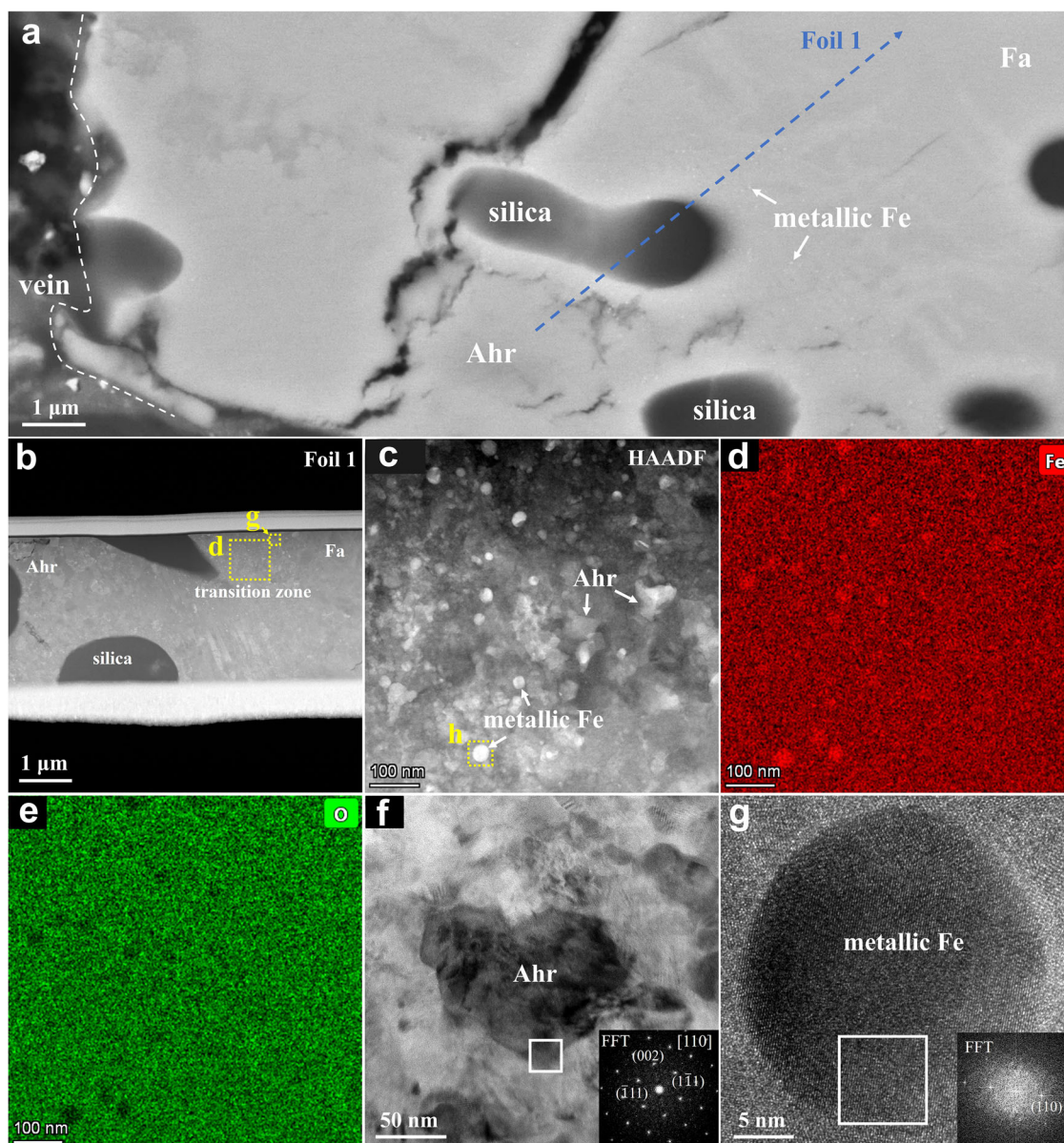


Fig. 2 | Microstructures of polycrystalline ahrensite and submicroscopic metallic iron. **a** Enlarged BSE image of ahrensite near the melt vein. The blue line indicates the location from which Foil 1 was extracted. Abundant submicroscopic metallic iron can be observed at the transition between ahrensite and fayalite. **b** HAADF image showing ahrensite, defect-rich fayalite, and the transition zone between fayalite and ahrensite. **c** HAADF image of the transition zone showing

metallic iron coexisting with ahrensite. **d, e** HAADF and corresponding EDS maps showing that the nanoparticles are Fe-rich and O-poor. **f** HRTEM image of ahrensite and its corresponding FFT pattern. **g** HRTEM image of metallic iron and its corresponding FFT pattern. Ahr ahrensite, Fa fayalite. White lines indicate the boundaries of the melt veins.

The plagioclase in the olivine gabbro has an anorthite content ($An = Ca/[Ca + Na]$) of approximately 92, and the corresponding transition pressure of plagioclase to maskelynite is ~ 25 GPa⁵⁰. Under the high-temperature conditions of the shock melt vein, the transition pressure should be lower than ~ 25 GPa. The presence of xieite near the melt vein requires the shock pressure and temperature to be >18 GPa and >1400 °C, respectively^{37,51}, whereas studies on α -cristobalite indicate that seifertite appears at pressure as low as ~ 11 GPa under nonhydrostatic conditions^{9,52}. Moreover, based on the majorite barometer⁵³, the required pressure for majorite is estimated to be 21.87 ± 0.55 GPa. Bridgmanite forms at pressures of 23–25 GPa^{49,54}, whereas the majorite-pyrope garnet and ringwoodite assemblage in the Allende meteorite requires approximately 20–24 GPa and ~ 2000 °C (Supplementary Fig. S7)⁵⁵. Therefore, we infer that NWA 3170 experienced shock pressures of 22–24 GPa and a temperature of approximately 2000 °C. The heterogeneity of high-pressure mineral assemblage indicates that the

P-T conditions of the experienced shock metamorphism were heterogeneously distributed. This is consistent with the results of other studies on high-pressure phases in meteorites^{31,56–58} and the quasichaotic nature of shock propagation in heterogeneous and/or porous materials⁵⁹.

The crystallization assemblages in the shock melt vein depend on the quench time and duration of the high shock pressure⁵⁹. The quench time for the shock vein, namely, the lag time between the crystallization of the edge and center of the vein, is estimated to be approximately 15 ms; this is based on the thermal conduction equation, namely, $t = L^2/\alpha$, where L is the width of the shock vein (calculated using the maximum width of melt vein of ~ 120 μm) and α is the thermal diffusion coefficient that is set to 10^{-6} $\text{m}^2 \text{s}^{-1}$ ⁶⁰. The rapid cooling rate is likely attributed to the presence of the shock vein being primarily at the interface between the breccia and the olivine gabbro, where the olivine gabbro acts as a heat sink. This is consistent with the results of numerical simulation of impact-induced

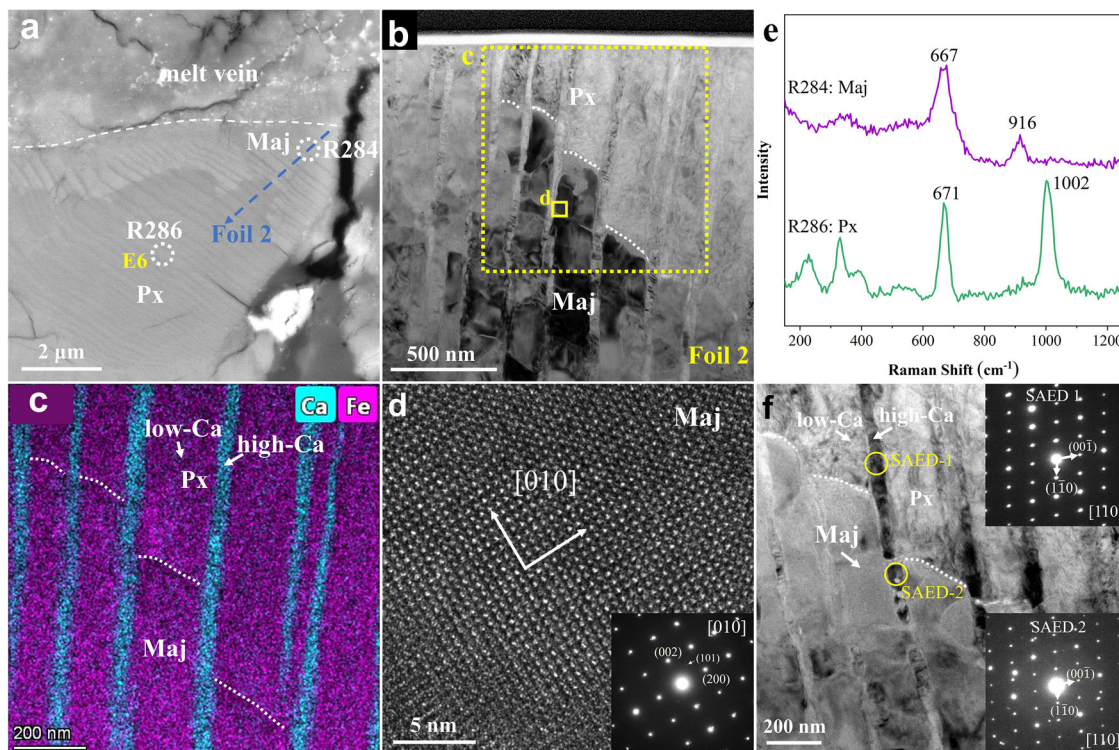


Fig. 3 | Microstructure of low-Ca majorite. **a** BSE image of majorite and pyroxene near the melt vein. The white circles indicate the location of Raman analysis. Yellow marker E6 indicates the position of EPMA measurement. The blue line represents the location from which Foil 2 was extracted. **b** TEM image of Foil 2 showing the lamellar texture of majorite. The white dashed lines indicate the boundary between

pyroxene and majorite. **c** STEM-EDS map showing the low-Ca and high-Ca pyroxene lamella. **d** HRTEM image and SAED pattern confirming the transformation of low-Ca pyroxene to majorite (garnet). **e** Raman spectra of pyroxene and majorite. **f** TEM image of lamellar high-Ca pyroxene and the SAED patterns of different regions. Maj majorite, Px pyroxene.

compaction in the poorly consolidated mix of chondrules and high-porosity matrix; that is, the matrix cools rapidly after the shock owing to the proximity to non-porous “cold” chondrules⁶¹. If the quench time is considerably longer than the duration of shock pressure, crystallization will occur during pressure release, and a difference in mineralogy will be observed between the vein edge and the vein center^{59,62}. As the entire shock vein contains high-pressure minerals that crystallized from the melt and shows no apparent back transformation to low-pressure polymorphs, the duration of shock pressure was at least 15 ms.

Formation mechanism of metallic iron

In this study, two distinct occurrences of metallic iron were identified. The first comprised tiny metallic iron nanoparticles embedded within ahrensite (Fig. 2). The disproportionation reaction ($3\text{Fe}^{2+} = 2\text{Fe}^{3+} + \text{Fe}^0$) could theoretically occur under extremely high temperature and pressure (i.e., approximately 20 GPa)^{63,64}. However, this hypothesis faces two inconsistencies. First, ahrensite decomposes into wuestite and stishovite at pressures above 17 GPa⁶⁵. Second, the metallic iron nanoparticles show preferential distribution in the ahrensite-fayalite transition zone, slightly away from the melt vein (Fig. 2a, b). This spatial distribution reveals that the formation pressure and temperature conditions are close to the threshold of high-pressure phase transition, but lower than those required for the disproportionation reaction. Instead, the observed Raman peak of bridgmanite glass (R216 in Fig. 1c) within this region supports an alternative decomposition pathway: fayalite/ahrensite decomposed into bridgmanite + metallic iron. The products were different from those in the previously reported dissociated olivine (vitrified bridgmanite + magnesiowüstite) in Martian meteorites and chondrites^{33,66,67}. Temperature and oxygen fugacity may be important controlling factors for this discrepancy, but further investigation is required.

The second type of metallic iron is present in the shock vein and sometimes coexists with sulfides (Fig. 4). This is similar to the occurrence in

the impact melt rocks and can be attributed to the liquid immiscibility between the sulfides and silicate melt during impact^{68,69}. The crystallized product is metallic iron, rather than magnesiowüstite, typically found in chondritic meteorites^{43,70}, probably because of the high vacuum and low oxygen fugacity on the lunar surface.

Both types of submicroscopic metallic iron are produced directly during the shock metamorphism, and are significantly different from those formed by space weathering (e.g., solar wind irradiation and micro-meteoroid impacts) on the surface of regolith grains^{17,21,71}. Metallic iron formed in this way may be ubiquitous on the lunar surface owing to the massive, large-scale impact events on the Moon. In particular, the early intense asteroid bombardment on the Moon may have generated substantial amounts of metallic iron. These metallic iron nanoparticles could aggregate and grow during subsequent multi-scale impact events, thereby considerably altering the spectral characteristics and magnetic properties of lunar samples.

Shock history of NWA 3170 and implications for high-pressure phases on the Moon

The unique high-pressure phase assemblage in NWA 3170 suggests that it experienced distinct impact histories compared with other lunar samples. The continuous shock vein in contact with olivine gabbro cuts across the gabbroic clast and breccia matrix, and therefore indicates that the shock vein formed after brecciation, namely, the latest impact event when the meteorite was ejected from the Moon. This inference is consistent with the chronological data of the NWA 773 clan meteorites to which NWA 3170 belongs. The Ar-Ar age of NWA 773 is ~2.9 Ga⁷², which is significantly younger than the Pb-Pb and U-Pb ages (~3.1 Ga) of baddeleyite and zircon^{26,73}, suggesting that they were excavated some time after ~2.9 Ga (Fig. 5)⁷⁴. After this collision, the ejecta of anorthositic crust, mare basalt, and gabbroic intrusive bodies were consolidated and brecciated to form the precursor lithology of NWA 3170⁷⁵. According to the total cosmic-ray exposure age, this meteorite

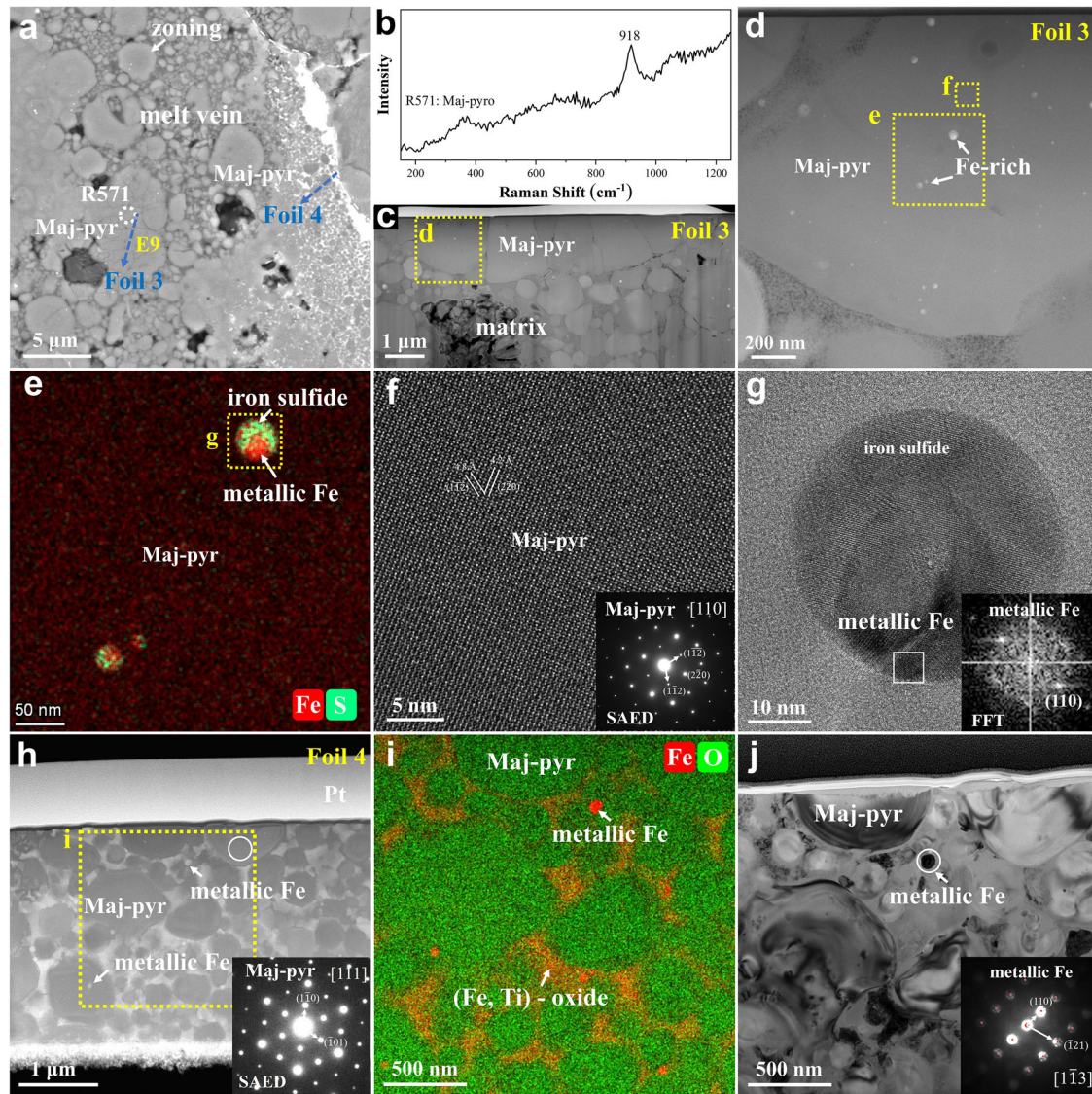


Fig. 4 | Microstructure of majorite-pyrope. **a** BSE image of majorite-pyrope (Maj-pyr) in the shock melt vein. The blue lines represent the locations where Foil 3 and Foil 4 were extracted. **b** Raman spectrum of majorite-pyrope (R571). **c** HAADF image showing the microstructure of Foil 3. **d** HAADF image of majorite-pyrope showing some bright nanoparticles within it. **e** The nanoparticles are composed of subgrains, including metallic iron and sulfide. **f** HRTEM image of majorite-pyrope

and its SAED pattern along the [110] zone axis. **g** HRTEM image of metallic iron and sulfide. The inset shows the FFT pattern of metallic iron. **h** HAADF image showing the microstructure of Foil 4. The inset shows the SAED pattern of majorite-pyrope along the [111] zone axis. **i** EDS map showing the metallic iron nanoparticles and (Fe, Ti)-oxides in the shock melt vein. **j** JTEM image of metallic iron and majorite-pyrope. The inset shows the CBED pattern of metallic iron along the [113] zone axis.

was subsequently ejected from the Moon at $<160 \text{ Ma}^{72,76}$. Our finding suggests that abundant high-pressure minerals were formed during this shock event.

We can estimate the approximate size of the second asteroid impactor on the Moon using the shock pressure ($\sim 24 \text{ GPa}$) and duration ($\sim 15 \text{ ms}$) based on the Rankine-Hugoniot relationship^{8,74,77}. The size was estimated to be 40 m, which would have formed a crater with a diameter of 274–607 m (calculation details are provided in Supplementary Text S1). The estimated crater size is consistent with the calculated result of 400–800 m, derived from the shock conditions of a paired meteorite NWA 2727⁷⁴. By comparing the geochemical composition and geochronological data with the remote-sensing datasets, the source region of the NWA 773 clan is most likely a fresh crater ($\sim 300 \text{ m}$ in diameter) on the edge of the Le Verrier D crater in Mare Imbrium, within the Procellarum KREEP Terrane⁷⁴.

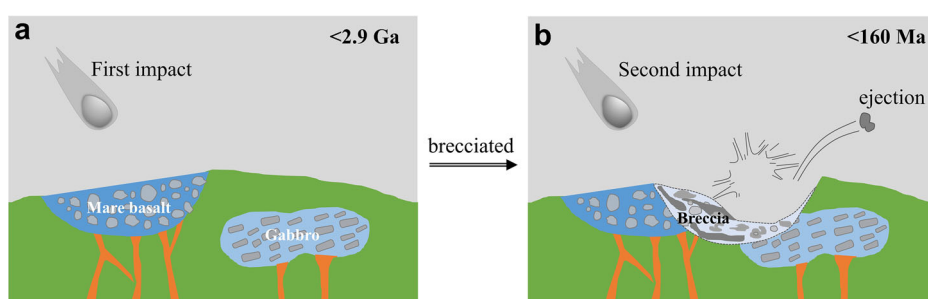
There are two possible reasons for the scarcity of high-pressure minerals in lunar meteorites. On the one hand, most lunar meteorites are launched at velocities below the escape velocity of the Earth-moon system

(2.78 km s^{-1})^{78,79}. When lunar ejecta are launched at higher velocities, they tend to enter independent heliocentric orbits, which substantially reduces the probability of reaching Earth⁷⁸. This suggests that lunar meteorites generally experience less intense shock metamorphism compared with Martian meteorites. On the other hand, the lunar surface comprises a layer of unconsolidated regolith covering the underlying bedrock. Shock recovery experiments reveal that temperature increases are greater in a porous materials than non-porous ones⁵⁹. For instance, an impact on a highly porous lunar regolith with an average peak pressure of $\sim 10 \text{ GPa}$ is capable of achieving a shock temperature of 1473 K^4 . However, high temperatures are not conducive to the preservation of most high-pressure minerals, such as causing the back transformation of wadsleyite to olivine⁸⁰. This could also be a key reason for the scarcity of high-pressure minerals in lunar samples. Hence, an impact with appropriate energy combined with a unique cooling history is a critical factor for the formation and preservation of high-pressure minerals in lunar samples. In addition, it has been noted that lunar meteorites generally show a higher level of shock than returned samples⁸¹.

Table 1 | High-pressure phases reported in lunar samples

Sample	High-pressure phases	References
NWA 3170	Stishovite, seifertite, ringwoodite, ahrensite, tuite, xieite, majorite, majorite-pyrope, vitrified bridgmanite	This study
SaU 169	Reidite	4
NWA 2977	Ringwoodite	5
NWA 479	Ringwoodite, wadsleyite	6
Asuka-881757	Coosite, stishovite	7
NWA 4734	Seifertite	8
NWA 2995, NWA 5000, NWA 8182, NWA 10203, NWA 10901, NWA 10253, NWA 10272, NWA 10782, NWA 11273, and NWA 13967	Tissintite	13,14
Oued Awlitis 001	Donwilhelmsite	15
Apollo	Stishovite	11
Chang'e-5	Stishovite, seifertite	9,10
Chang'e-6	Coosite	12

Fig. 5 | Schematics of the impact history of meteorite NWA 3170. a The sample was brecciated after the first impact. **b** The meteorite was ejected from the Moon after a large second impact, after ref. 75.



One explanation for this phenomenon is location bias, wherein lunar meteorites represent a random global sampling, whereas returned samples originate from limited regions on the lunar surface⁸¹. Alternatively, it could be attributed to differences in sample collection, as lunar meteorites were ejected from the Moon by impacts rather than being collected directly. We emphasize the need for further studies of high-pressure polymorphs in lunar meteorites (e.g., NWA 773 clan) using advanced microanalysis techniques. This can reveal new shock effects on the Moon and enhance our understanding of the behavior of materials under extreme conditions.

Materials and methods

SEM

Petrographic observations of NWA 3170 were conducted via backscattered electron (BSE) imaging, using the Thermo Fisher Apreo S and Nova 450 field emission scanning electron microscopes (SEMs) equipped with energy dispersive X-ray spectroscopy (EDS) detectors at the Institute of Geology and Geophysics, Chinese Academy of Sciences (IGGCAS). A large area BSE image was acquired using the MAPS software. The instruments were operated at accelerating voltages of 10–20 kV with beam currents of 1.6–6.4 nA. Electron back-scattered diffraction (EBSD) data were collected with an Oxford Symmetry EBSD detector and processed with Aztec Crystal to determine the mineral phases.

EPMA

Quantitative chemical compositions of the minerals were determined using a JEOL 8100 electron probe microanalyzer (EPMA) with wavelength dispersive spectrometers (WDS) at IGGCAS. It was operated at an accelerating voltage of 15 kV, a probe current of 20 nA, and spot size of approximately 1–2 μm spot size. The following natural and synthetic mineral standards were used: albite for Na, Si, and Al; diopside for Mg and Ca; fluorite for F; apatite for P; tugtupite for Cl; hematite for Fe; bustamite for Mn; sanidine for K; rutile for Ti; and Cr_2O_3 for Cr. All data were processed using the ZAF correction procedure.

Raman

Raman spectra of the minerals were acquired using a WITec alpha 300 R confocal Raman system. An optical microscope with 100 \times objective lens (Numerical Aperture: 0.9) was used to focus the 532-nm excitation laser beam onto the sample. A laser power of approximately 2 mW was used to identify the high-pressure minerals.

FIB and TEM

The ultrathin foils (~100 nm thick) were prepared using a Zeiss Auriga Compact focused ion beam (FIB) microscope equipped with an Omniprobe AutoProbe 200 micromanipulator. Ion beam milling and final polishing were performed at 5–30 kV and various beam currents (20 pA to 4 nA). Prior to FIB cutting, Pt was deposited to protect the sample surface from FIB Ga^+ damage. The microstructures of the foils were examined via transmission electron microscopy (TEM) using JEOL JEM-2100 and Thermo Fisher Talos 200X instruments. The crystallographic structures were analyzed through selected area electron diffraction (SAED), convergent-beam electron diffraction (CBED), high-resolution TEM (HRTEM) imaging, and high-angle annular dark field scanning transmission electron microscopy (HAADF-STEM). EDS point analyses and STEM-EDS mapping were used to determine the chemical compositions of the nanoscale phases. Semi-quantitative composition analysis was conducted using the Oxford Aztec and Thermo Scientific Velox software.

Estimation of impactor size and crater diameter

The size of the impactor and crater can be estimated from the parameters of launch impact based on the Rankine–Hugoniot's relations^{77,82}. Detailed procedures are provided in Supplementary Text S1.

Data availability

Data used in the study are presented in the main manuscript and are also available through Mendeley Data (<https://doi.org/10.17632/4zrsfhkfv.1>).

Received: 6 May 2025; Accepted: 3 October 2025;
Published online: 17 November 2025

References

- Zhu, J. et al. Shock metamorphism of lunar minerals. *Space. Sci. Technol.* **4**, 0124 (2024).
- Stöffler, D., Keil, K. & Scott, E. R. D. Shock metamorphism of ordinary chondrites. *Geochim. Cosmochim. Acta* **55**, 3845–3867 (1991).
- Tomioka, N. & Miyahara, M. High-pressure minerals in shocked meteorites. *Meteorit. Planet. Sci.* **52**, 2017–2039 (2017).
- Xing, W. et al. Discovery of reidite in the lunar meteorite Sayh al Uhaymir 169. *Geophys. Res. Lett.* **47**, e2020GL089583 (2020).
- Zhang, A. C. et al. Petrogenesis of lunar meteorite Northwest Africa 2977: constraints from in situ microprobe results. *Meteorit. Planet. Sci.* **45**, 1929–1947 (2010).
- Barrat, J. et al. Lithium behavior during cooling of a dry basalt: an ion-microprobe study of the lunar meteorite Northwest Africa 479 (NWA 479). *Geochim. Cosmochim. Acta* **69**, 5597–5609 (2005).
- Ohtani, E. et al. Coesite and stishovite in a shocked lunar meteorite, Asuka-881757, and impact events in lunar surface. *Proc. Natl. Acad. Sci. USA* **108**, 463–466 (2011).
- Miyahara, M. et al. Discovery of seifertite in a shocked lunar meteorite. *Nat. Commun.* **4**, 1737 (2013).
- Pang, R. et al. New occurrence of seifertite and stishovite in Chang'E-5 regolith. *Geophys. Res. Lett.* **49**, e2022GL098722 (2022).
- Qiu, M. et al. Discovery of a highly shocked alkali suite clast in the Chang'e-5 lunar soils. *Icarus* **429**, 116448 (2025).
- Kaneko, S. et al. Discovery of stishovite in Apollo 15299 sample. *Am. Mineralogist* **100**, 1308–1311 (2015).
- Zhou, Z. et al. Discovery of coesite on the lunar farside. *J. Geophys. Res. Planets* **130**, e2025JE009052 (2025).
- Zhang, A. C. et al. Widespread tissantite in strongly shock-lithified lunar regolith breccias. *Geophys. Res. Lett.* **48**, e2020GL091554 (2021).
- Wittmann, A. et al. Tissantite-II in lunar meteorite Northwest Africa 13967: implications for the high pressure/temperature mineralogy of the lunar regolith. *Meteorit. Planet. Sci.* **60**, 484–505 (2025).
- Fritz, J. et al. Donwilhelmsite, $[\text{CaAl}_4\text{Si}_2\text{O}_{11}]$, a new lunar high-pressure Ca-Al-silicate with relevance for subducted terrestrial sediments. *Am. Mineral.* **105**, 1704–1711 (2020).
- Hapke, B. Space weathering from Mercury to the asteroid belt. *J. Geophys. Res. Planets* **106**, 10039–10073 (2001).
- Pieters, C. M. & Noble, S. K. Space weathering on airless bodies. *J. Geophys. Res.: Planets* **121**, 1865–1884 (2016).
- Gu, L. et al. Space weathering of the Chang'e-5 lunar sample from a mid-high latitude region on the Moon. *Geophys. Res. Lett.* **49**, e2022GL097875 (2022).
- Keller, L. P. & McKay, D. S. The nature and origin of rims on lunar soil grains. *Geochim. Cosmochim. Acta* **61**, 2331–2341 (1997).
- Keller, L. P. & McKay, D. S. Discovery of vapor deposits in the lunar regolith. *Science* **261**, 1305–1307 (1993).
- Denevi, B. W. et al. Space weathering at the Moon. *Rev. Mineral. Geochem.* **89**, 611–650 (2023).
- Burgess, K. D. & Stroud, R. M. Phase-dependent space weathering effects and spectroscopic identification of retained helium in a lunar soil grain. *Geochim. Cosmochim. Acta* **224**, 64–79 (2018).
- Pieters, C. M., Taylor, L. A. & Noble, S. K. Space weathering on airless bodies: resolving a mystery with lunar samples. *Meteorit. Planet. Sci.* **35**, 1101–1107 (2000).
- Longhi, J. Experimental petrology and petrogenesis of mare volcanics. *Geochim. Cosmochim. Acta* **56**, 2235–2251 (1992).
- Gopon, P. et al. Ultra-reduced phases in Apollo 16 regolith: combined field emission electron probe microanalysis and atom probe tomography of submicron Fe-Si grains in Apollo 16 sample 61500. *Meteorit. Planet. Sci.* **52**, 1941–1962 (2017).
- Shaulis, B., Righter, M., Lapen, T., Jolliff, B. & Irving, A. 3.1 Ga crystallization age for magnesian and ferroan gabbro lithologies in the Northwest Africa 773 clan of lunar meteorites. *Geochim. Cosmochim. Acta* **213**, 435–456 (2017).
- Merle, R. E. et al. Pb-Pb ages and initial Pb isotopic composition of lunar meteorites: NWA 773 clan, NWA 4734, and Dhofar 287. *Meteorit. Planet. Sci.* **55**, 1808–1832 (2020).
- Valencia, S. N., Jolliff, B. L. & Korotev, R. L. Petrography, relationships, and petrogenesis of the gabbroic lithologies in Northwest Africa 773 clan members Northwest Africa 773, 2727, 3160, 3170, 7007, and 10656. *Meteorit. Planet. Sci.* **54**, 2083–2115 (2019).
- Jolliff, B. L., Korotev, R. L., Zeigler, R. A. & Floss, C. Northwest Africa 773: lunar mare breccia with a shallow-formed olivine-cumulate component, inferred very-low-Ti (VLT) heritage, and a KREEP connection. *Geochim. Cosmochim. Acta* **67**, 4857–4879 (2003).
- Lorenzetti, S., Busemann, H. & Eugster, O. Regolith history of lunar meteorites. *Meteorit. Planet. Sci.* **40**, 315–327 (2005).
- Gu, L. et al. Occurrence of tuite and ahrensites in Zagami and their significance for shock-histories recorded in martian meteorites. *Am. Mineral. J. Earth Planet. Mater.* **107**, 1018–1029 (2022).
- Feng, L., Lin, Y., Hu, S., Xu, L. & Miao, B. Estimating compositions of natural ringwoodite in the heavily shocked Grove Mountains 052049 meteorite from Raman spectra. *Am. Mineral.* **96**, 1480–1489 (2011).
- Ma, C. et al. Ahrensites, $\gamma\text{-Fe}_2\text{SiO}_4$, a new shock-metamorphic mineral from the Tissint meteorite: Implications for the Tissint shock event on Mars. *Geochim. Cosmochim. Acta* **184**, 240–256 (2016).
- Baziotis, I. P. et al. The Tissint Martian meteorite as evidence for the largest impact excavation. *Nat. Commun.* **4**, 1404 (2013).
- Martinez, M., Brearley, A. J., Trigo-Rodríguez, J. M. & Llorca, J. New observations on high-pressure phases in a shock melt vein in the Villabeto de la Peña meteorite: Insights into the shock behavior of diopside. *Meteorit. Planet. Sci.* **54**, 2845–2863 (2019).
- Xie, X., Gu, X. & Chen, M. An occurrence of tuite, $\gamma\text{-Ca}_3(\text{PO}_4)_2$, partly transformed from Ca-phosphates in the Suizhou meteorite. *Meteorit. Planet. Sci.* **51**, 195–202 (2016).
- Ishii, T. et al. High-pressure phase transitions in FeCr_2O_4 and structure analysis of new post-spinel FeCr_2O_4 and $\text{Fe}_2\text{Cr}_2\text{O}_5$ phases with meteoritical and petrological implications. *Am. Mineral.* **99**, 1788–1797 (2014).
- Ma, C. et al. Chenmingite, FeCr_2O_4 in the CaFe_2O_4 -type structure, a shock-induced, high-pressure mineral in the Tissint martian meteorite. *Am. Mineral.* **104**, 1521–1525 (2019).
- Ohtani, E. et al. Formation of high-pressure minerals in shocked L6 chondrite Yamato 791384: constraints on shock conditions and parent body size. *Earth Planet. Sci. Lett.* **227**, 505–515 (2004).
- Tomioka, N. et al. Microstructures and structural phase transition in $(\text{Mg}, \text{Fe})\text{SiO}_3$ majorite. *Eur. J. Mineral.* **14**, 7–14 (2002).
- Sinogeikin, S. V. & Bass, J. D. Elasticity of pyrope and majorite–pyrope solid solutions to high temperatures. *Earth Planet. Sci. Lett.* **203**, 549–555 (2002).
- Bazhan, I. S., Litasov, K. D., Ohtani, E. & Ozawa, S. Majorite-olivine-high-Ca pyroxene assemblage in the shock-melt veins of Pervomaisky L6 chondrite. *Am. Mineral.* **102**, 1279–1286 (2017).
- Chen, M., Sharp, T. G., El Goresy, A., Wopenka, B. & Xie, X. The majorite–pyrope+magnesiowüstite assemblage: Constraints on the history of shock veins in chondrites. *Science* **271**, 1570–1573 (1996).
- El Goresy, A. et al. Shock-induced deformation of Shergottites: shock-pressures and perturbations of magmatic ages on Mars. *Geochim. Cosmochim. Acta* **101**, 233–262 (2013).
- Xie, X., Zhai, S., Chen, M. & Yang, H. Tuite, $\gamma\text{-Ca}_3(\text{PO}_4)_2$, formed by chlorapatite decomposition in a shock vein of the Suizhou L6 chondrite. *Meteorit. Planet. Sci.* **48**, 1515–1523 (2013).
- Murayama, J. K., Nakai, S., Kato, M. & Kumazawa, M. A dense polymorph of $\text{Ca}_3(\text{PO}_4)_2$: a high pressure phase of apatite

- decomposition and its geochemical significance. *Phys. Earth Planet. Inter.* **44**, 293–303 (1986).
47. Miyahara, M., Tomioka, N. & Bindi, L. Natural and experimental high-pressure, shock-produced terrestrial and extraterrestrial materials. *Prog. Earth Planet. Sci.* **8**, 59 (2021).
 48. Miyahara, M., Ohtani, E., El Goresy, A., Ozawa, S. & Gillet, P. Phase transition processes of olivine in the shocked Martian meteorite Tissint: clues to origin of ringwoodite-, bridgmanite- and magnesiowüstite-bearing assemblages. *Phys. Earth Planet. Inter.* **259**, 18–28 (2016).
 49. Richet, P. & Gillet, P. Pressure-induced amorphization of minerals: a review. *Eur. J. Mineral. Ohne Beih.* **9**, 907–934 (1997).
 50. Fritz, J., Assis Fernandes, V., Greshake, A., Holzwarth, A. & Böttger, U. On the formation of diaplectic glass: shock and thermal experiments with plagioclase of different chemical compositions. *Meteorit. Planet. Sci.* **54**, 1533–1547 (2019).
 51. Chen, M., Shu, J. & Mao, H.-K. Xieite, a new mineral of high-pressure FeCr_2O_4 polymorph. *Chin. Sci. Bull.* **53**, 3341–3345 (2008).
 52. Kubo, T., Kato, T., Higo, Y. & Funakoshi, K. -i Curious kinetic behavior in silica polymorphs solves seifertite puzzle in shocked meteorite. *Sci. Adv.* **1**, e1500075 (2015).
 53. Collerson, K. D. et al. Majoritic garnet: a new approach to pressure estimation of shock events in meteorites and the encapsulation of sub-lithospheric inclusions in diamond. *Geochim. Cosmochim. Acta* **74**, 5939–5957 (2010).
 54. Tschauner, O. et al. Discovery of bridgmanite, the most abundant mineral in Earth, in a shocked meteorite. *Science* **346**, 1100–1102 (2014).
 55. Agee, C., Li, J., Shannon, M. & Circone, S. Pressure-temperature phase diagram for the Allende meteorite. *J. Geophys. Res. Solid Earth* **100**, 17725–17740 (1995).
 56. Gillet, P., El Goresy, A., Beck, P. & Chen, M. High-pressure mineral assemblages in shocked meteorites and shocked terrestrial rocks: mechanisms of phase transformations and constraints to pressure and temperature histories. *Geol. Soc. Am. Special Pap.* **421**, (2007).
 57. Walton, E. L., Sharp, T. G., Hu, J. & Filiberto, J. Heterogeneous mineral assemblages in Martian meteorite Tissint as a result of a recent small impact event on Mars. *Geochim. Cosmochim. Acta* **140**, 334–348 (2014).
 58. Xie, Z., Sharp, T. G. & DeCarli, P. S. High-pressure phases in a shock-induced melt vein of the Tenham L6 chondrite: Constraints on shock pressure and duration. *Geochim. Cosmochim. Acta* **70**, 504–515 (2006).
 59. Sharp, T. G. & DeCarli, P. S. Shock effects in meteorites. *Meteor. Early Sol. Syst. II* **943**, 653–677 (2006).
 60. Fritz, J. & Greshake, A. High-pressure phases in an ultramafic rock from Mars. *Earth Planet. Sci. Lett.* **288**, 619–623 (2009).
 61. Bland, P. et al. Pressure-temperature evolution of primordial solar system solids during impact-induced compaction. *Nat. Commun.* **5**, 5451 (2014).
 62. Zhang, T. et al. Formation mechanisms of ringwoodite: clues from the Martian meteorite Northwest Africa 8705. *Earth Planets Space* **73**, 1–18 (2021).
 63. Ma, C., Tschauner, O., Beckett, J. R. & Prakapenka, V. B. New high-pressure Fe-Ti oxide minerals in the Shergotty Martian meteorite: feiite, $\text{Fe}^{2+}_2(\text{Fe}^{2+}\text{Ti}^{4+})\text{O}_5$, liuite, FeTiO_3 , and tschaunerite, $(\text{Fe}^{2+}\text{Ti}^{4+})\text{O}_4$. *Meteorit. Planet. Sci.* **60**, 375–391 (2025).
 64. Bindi, L., Shim, S.-H., Sharp, T. G. & Xie, X. Evidence for the charge disproportionation of iron in extraterrestrial bridgmanite. *Sci. Adv.* **6**, eaay7893 (2020).
 65. Akaogi, M., Miyazaki, N., Tajima, T. & Kojitani, H. Post-spinel transition of Fe_2SiO_4 ahrensite at high pressure and high temperature. *Phys. Chem. Miner.* **50**, 23 (2023).
 66. Miyahara, M. et al. Natural dissociation of olivine to $(\text{Mg,Fe})\text{SiO}_3$ perovskite and magnesiowüstite in a shocked Martian meteorite. *Proc. Natl. Acad. Sci.* **108**, 5999–6003 (2011).
 67. Tiwari, K., Ghosh, S., Miyahara, M. & Ray, D. Shock-induced incongruent melting of olivine in Kamargaon L6 chondrite. *Geophys. Res. Lett.* **48**, e2021GL093592 (2021).
 68. Hamann, C. et al. Silicate liquid immiscibility in impact melts. *Meteorit. Planet. Sci.* **53**, 1594–1632 (2018).
 69. Yin, C. et al. Shock induced metal globules in Chang'e-5 impact melt splash and implication for the coalescence growth of submicroscopic metal particles in lunar soil. *J. Geophys. Res.: Planets* **130**, e2024JE008733 (2025).
 70. Tomioka, N. & Fujino, K. Akimotoite, $(\text{Mg, Fe})\text{SiO}_3$, a new silicate mineral of the ilmenite group in the Tenham chondrite. *Am. Mineral.* **84**, 267–271 (1999).
 71. Gu, L. et al. Submicron-scale craters on Chang'e-5 lunar soils: records of complex space weathering processes. *Geochim. Cosmochim. Acta* **398**, 139–151 (2025).
 72. Fernandes, V. A., Burgess, R. & Turner, G. ^{40}Ar - ^{39}Ar chronology of lunar meteorites Northwest Africa 032 and 773. *Meteorit. Planet. Sci.* **38**, 555–564 (2003).
 73. Borg, L. E. et al. Mechanisms for incompatible-element enrichment on the Moon deduced from the lunar basaltic meteorite Northwest Africa 032. *Geochim. Cosmochim. Acta* **73**, 3963–3980 (2009).
 74. Nagaoka, H. et al. Investigation of the source region of the lunar-meteorite group with the remote sensing datasets: implication for the origin of mare volcanism in Mare Imbrium. *Icarus* **370**, 114690 (2021).
 75. Kayama, M. et al. Discovery of moganite in a lunar meteorite as a trace of H_2O ice in the Moon's regolith. *Sci. Adv.* **4**, eaar4378 (2018).
 76. Eugster, O. & Lorenzetti, S. Exposure history of some differentiated and lunar meteorites. *Meteorit. Planet. Sci.* **36**, A54 (2001).
 77. Melosh, H. J. *Impact Cratering: A Geologic Process* (The University of California, 1989).
 78. Rubin, A. E. Maskelynite in asteroidal, lunar and planetary basaltic meteorites: an indicator of shock pressure during impact ejection from their parent bodies. *Icarus* **257**, 221–229 (2015).
 79. Gladman, B. J., Burns, J. A., Duncan, M. J. & Levison, H. F. The dynamical evolution of lunar impact ejecta. *Icarus* **118**, 302–321 (1995).
 80. Hu, J. P. & Sharp, T. G. Back-transformation of high-pressure minerals in shocked chondrites: low-pressure mineral evidence for strong shock. *Geochim. Cosmochim. Acta* **215**, 277–294 (2017).
 81. Osinski, G. R. et al. Lunar impact features and processes. *Rev. Mineral. Geochem.* **89**, 339–371 (2023).
 82. O'Keefe, J. D. & Ahrens, T. J. Planetary cratering mechanics. *J. Geophys. Res. Planets* **98**, 17011–17028 (1993).

Acknowledgements

We are grateful to Xiaoying Liu, Xi Ma, Bin Su, Runlian Pang, Fei Su, Xiaopeng Yang, and Qiuli Li for their assistance with sample analysis and manuscript preparation. We appreciate the constructive suggestions and comments from the reviewers, Axel Wittmann and 2 anonymous reviewers. The meteorite Northwest Africa 3170 was purchased from the meteorite market and is owned by Professor Lin Yangting, one of the corresponding authors. This study was funded by the National Natural Science Foundation of China (grant numbers 42230206, 42241105, and 42103035) and the Key Research Program of the Institute of Geology and Geophysics, CAS (IGGCAS-202101 and IGGCAS-202401).

Author contributions

L.G. Data curation, methodology, investigation, writing—original draft, Writing-review and editing, funding acquisition. N.W. Investigation, writing—review, and editing. Y.L. Writing-review and editing, conceptualization, supervision, funding acquisition. H.T. Investigation, writing—review and editing. X.T. Methodology, writing—review and editing. Z.Z. Writing—review

and editing. X.L. Methodology, writing—review and editing. L.J. Methodology, writing—review and editing. Y.X. Writing—review and editing. S.H. Writing—review and editing. J.L. Writing—review and editing, supervision.

Competing interests

The authors declare no competing interests.

Additional information

Supplementary information The online version contains supplementary material available at

<https://doi.org/10.1038/s43247-025-02876-z>.

Correspondence and requests for materials should be addressed to Lixin Gu, Yangting Lin or Jinhua Li.

Peer review information *Communications Earth & Environment* thanks Axel Wittmann and the other, anonymous, reviewer(s) for their contribution to the peer review of this work. Primary Handling Editors: Claire Nichols, Joe Aslin and Alice Drinkwater. A peer review file is available.

Reprints and permissions information is available at <http://www.nature.com/reprints>

Publisher's note Springer Nature remains neutral with regard to jurisdictional claims in published maps and institutional affiliations.

Open Access This article is licensed under a Creative Commons Attribution-NonCommercial-NoDerivatives 4.0 International License, which permits any non-commercial use, sharing, distribution and reproduction in any medium or format, as long as you give appropriate credit to the original author(s) and the source, provide a link to the Creative Commons licence, and indicate if you modified the licensed material. You do not have permission under this licence to share adapted material derived from this article or parts of it. The images or other third party material in this article are included in the article's Creative Commons licence, unless indicated otherwise in a credit line to the material. If material is not included in the article's Creative Commons licence and your intended use is not permitted by statutory regulation or exceeds the permitted use, you will need to obtain permission directly from the copyright holder. To view a copy of this licence, visit <http://creativecommons.org/licenses/by-nc-nd/4.0/>.

© The Author(s) 2025